communications physics

ARTICLE

https://doi.org/10.1038/s42005-024-01538-4 OPEN

# Extreme-value analysis of intracellular cargo transport by motor proteins

Takuma Naoi[1], Yuki Kagawa[1], Kimiko Nagino[1], Shinsuke Niwa[2] & Kumiko Hayashi[1,3]✉

The mechanisms underlying the chemo-mechanical coupling of motor proteins is usually described by a set of force-velocity relations that reflect the different mechanisms responsible for the walking behavior of such proteins on microtubules. However, the convexity of such relations remains controversial depending on the species, and in vivo experiments are inaccessible due to the complexity of intracellular environments. As alternative tool to investigate such mechanism, Extreme-value analysis (EVA) can offer insight on the deviations in the data from the median of the probability distributions. Here, we rely on EVA to investigate the motility functions of nanoscale motor proteins in neurons of the living worm *Caenorhabditis elegans* (*C. elegans*), namely the motion of kinesin and dynein along microtubules. While the essential difference between the two motors cannot be inferred from the mean velocities, such becomes evident in the EVA plots. Our findings extend the possibility and applicability of EVA for analysing motility data of nanoscale proteins in vivo.

[1] Department of Applied Physics, Graduate school of Engineering, Tohoku University, Aramaki, Aoba 6-6-05, Aoba-ku, Sendai, Miyagi 980-8579, Japan. [2] Frontier Research Institute for Interdisciplinary Sciences, Tohoku University, Aramaki, Aoba 6-3, Aoba-ku, Sendai, Miyagi 980-0845, Japan. [3] Institute for Solid State Physics, The University of Tokyo, Kashiwano-ha 5-1-5, Kashiwa, Chiba 277-8581, Japan. ✉email: hayashi@issp.u-tokyo.ac.jp

Motor protein is a general term for proteins that move and function using energy obtained from adenosine triphosphate (ATP) hydrolysis; these are elaborate nanosized molecular machines that function in our bodies. For example, while myosin swings its lever arm to cause muscle contraction[1,2], kinesin and dynein walk along the microtubules to transport intracellular materials[3,4], and a part of $F_oF_1$ synthase, $F_1$ rotates by hydrolyzing ATP molecules[5]. The physical properties of motor proteins, such as force and velocity, have been investigated by in-vitro single-molecule experiments, in which the functions of motor proteins consisting of minimal complexes were analyzed in glass chambers[6–12]. The mechanisms underlying the chemo-mechano coupling of motor proteins have been clarified by manipulating single molecules using optical tweezers[6–12], magnetic tweezers[13,14], and electric fields[15,16]. Force-velocity relationships for kinesin and dynein have been clarified based on in-vitro single-molecule studies using optical tweezers. The difference in the convexity of force-velocity relationships reflects the different mechanisms underlying the walking behavior of motor proteins on microtubules. The force-velocity relationship for kinesin is concave-down[6], while concave-up force-velocity relationships were found for dynein[9,10,17]. However, its convexity remains controversial depending on the species[7–10,12,18].

Because motor proteins function fully in the intracellular environment and are equipped with accessory proteins, the investigation of motor proteins in vivo is as important as in-vitro single-molecule experiments; however, it is difficult to manipulate motors using optical tweezers in complex intracellular environments. As alternative tool to investigate such mechanism, Extreme-value analysis (EVA) can offer insight on the deviations in the data from the median of the probability distributions. EVA[19,20] is a statistical tool that can retrieve information regarding the extreme values of observed data that deviate from the median of probability distributions. Such extreme values are important in various topics, such as disaster prevention[21,22], finance[23], safety estimation[24], sports[25,26], human lifespan[27,28], and the recent pandemic[29]. Recently, its applications in the biological data analysis has also become active[30]. Our findings indicate that, without direct manipulation, EVA effectively reveals information about the convexity of the force-velocity relationship for motor proteins in vivo.

Here, we extended the use of EVA to investigate nanoscale phenomena associated with the function of motor proteins inside cells, focusing on the in vivo velocity of synaptic cargo transport performed by the motor proteins kinesin (UNC-104[31,32]) and dynein[33] in the axons of motor neurons of living *Caenorhabditis elegans* (*C. elegans*), a model organism in neuroscience. As the axons of these worms are sufficiently long, this in vivo system is appropriate for investigating intracellular cargo transport. Synaptic materials packed as cargo are delivered to the synaptic region of neurons via kinesin-mediated anterograde transport, and unnecessary materials that accumulate in the synaptic region are returned to the cell body via dynein-mediated retrograde transport (Fig. 1a). Since the bodies of worms are transparent and their body movement is suppressed by anesthesia, the motion of fluorescently labeled synaptic cargos in living worms can be observed by fluorescence microscopy (Fig. 1b)[34]. Velocities were measured from recorded images (Fig. 1b). By applying EVA to the velocity data of the intracellular cargo transport, we investigated the force-velocity relationship between kinesin and dynein. We found that difference in the parameters of the generalized extreme value distributions and return level plots of the EVA. The difference was then related to the force-velocity relationship of kinesin and dynein by using simulations.

## Results

**Transport velocity of synaptic cargos**. Fluorescence images of green fluorescence protein (GFP)-labeled synaptic cargo transported by motor proteins were captured using a 150× objective lens and an sCMOS camera at 10 frames per second (see Methods). The body movements of *C. elegans* worms were suppressed under anesthesia. For only the motionless worms, kymograph analysis of the recorded images was performed using the multi kymograph module in ImageJ[35] (Fig. 1b). Although we observed 562 worms totally, the velocity values of the moving cargo were collected from 232 worms, revealing that transport velocities were not observed in the rest of the worms because of the body movement and the obscurity of fluorescence movies.

The velocity values were calculated as the slopes of the trajectories of the fluorescently labeled cargo in the kymograph images (Fig. 1b). Typically, a cargo exhibits a moving motion at a constant velocity, and pauses, and rarely reverses its direction (Fig. 1c). Constant velocity segments (CVSs) were assumed to be unaffected by the other motor proteins much based on other experimental studies[36,37]. It means that the tug-of-war between the two motors, kinesin and dynein[37,38], was not considered for CVSs in this study, and that we supported the motor coordination model, in which adaptor proteins that connect motors with cargos deactivate opposing motors[33].

Figure 1d shows the histograms of the measured velocities $\{v^i\}$ ($i = 1, \cdots, n$ where $n = 2091$ for anterograde transport from 228 worms and $n = 1113$ for retrograde transport from 217 worms). The mean velocities were 1.6±0.5(SE) μm/s and 1.8±0.7(SE) μm/s for anterograde and retrograde transport, respectively. These values are similar to those reported for the same neurons in *C. elegans* worms[39–41] (higher than the values obtained by the in vitro single-molecule experiments). In the in vivo case, the velocity values varied widely as revealed by the histogram (Fig. 1d). This broad variation was considered to originate from the cargo size difference (Fig. 1e) based on our previous study[42]. Here, the functional form of distribution of the cargo size was estimated from that of the fluorescence intensity (FI) of the cargo (Fig. 1e) through the relation $\mathrm{FI} \propto 4\pi r^2$ ($r$: radius of cargo), *i.e.*, $r \propto \sqrt{\mathrm{FI}}$, assuming that the fluorescent proteins labeling a cargo are uniformly distributed on its surface.

**Application of EVA to assess transport velocity data**. In this study, one block of EVA was considered as a single worm. Approximately $M = 5$–$20$ velocity values were observed for each worm, from which the largest value ($v^i_{\max}$) was selected. (Note that the variability and small size of $M$ is discussed in the discussion section and Fig. S1.) Using $\{v^i_{\max}\}$ ($i = 1, \cdots, n$ where $n = 228$ for anterograde transport and $n$=217 for retrograde transport), the return-level plot was investigated (Fig. 2a). The two axes of the return level plot represent the return period $r_p$ and return level $z_p$. For a given probability $p$, $r_p = -\{\log(1-p)\}^{-1}$, and $z_p$ is defined by the generalized extreme value distribution as $1 - p = G(z_p)$, where

$$G\left(z_p\right) = \exp\left[-\left\{1 + \xi\left(\frac{z_p - \mu}{\sigma}\right)\right\}^{-1/\xi}\right]. \quad (1)$$

Note that $z_p$ and $r_p$ represent $\{\hat{v}^i_{\max}\}$ and the number of samples, respectively. Here $\{\hat{v}^i_{\max}\}$ is the rearranged data of $\{v^i_{\max}\}$, such that $\hat{v}^1_{\max} \le \hat{v}^2_{\max} \le \cdots \le \hat{v}^n_{\max}$. From EVA by using the ismev and evd packages in R[43], we obtained parameters of the generalized extreme value distribution $\xi$, $\mu$, and $\sigma$ in Eq. (1) (Table S1). We found that $\xi < 0$ for anterograde transport and $\xi \sim 0$ for retrograde transport. The return level plot for anterograde transport shows a convergent behavior as $r_p$ becomes larger (Fig. 2a), a property specific to a Weibull

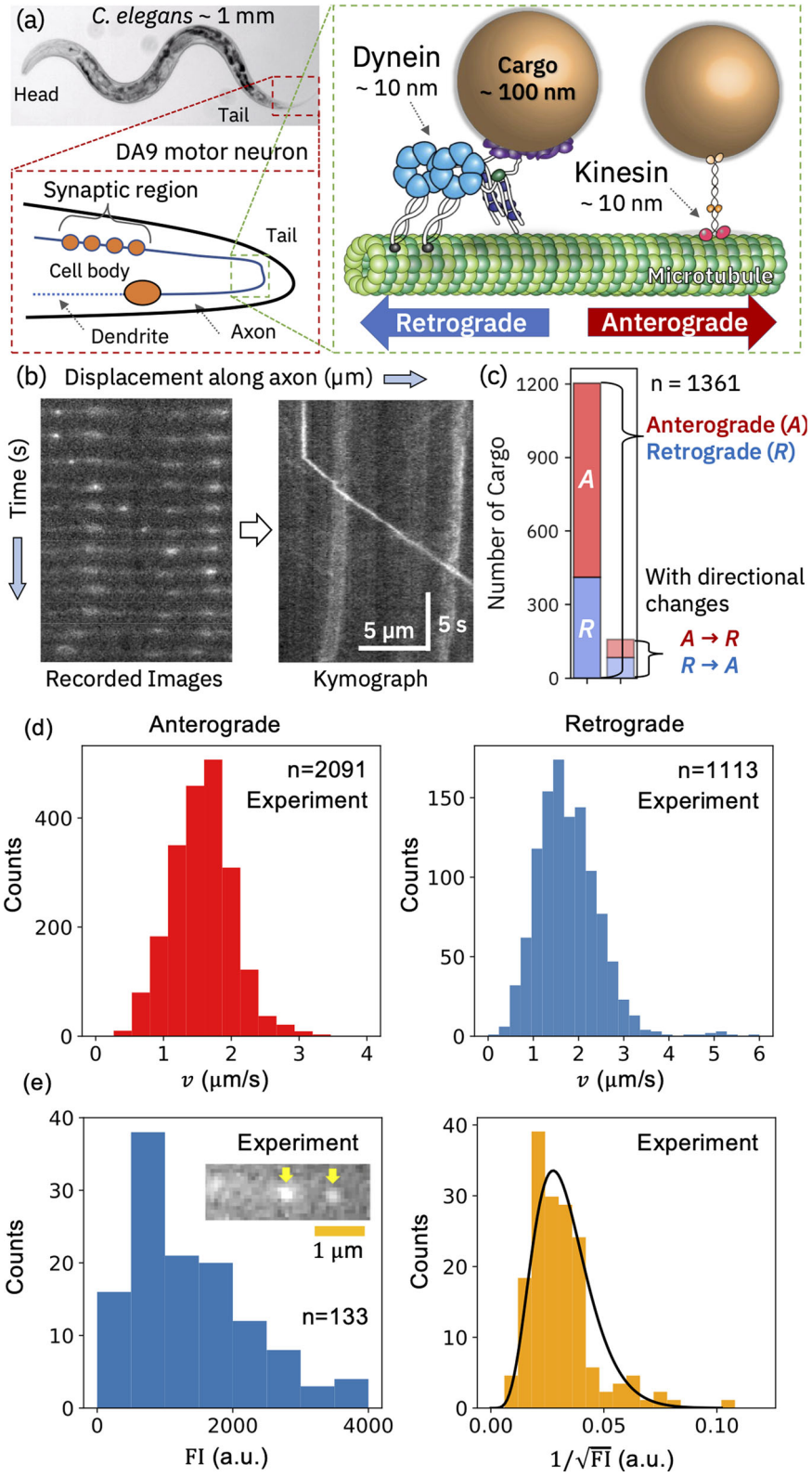


**Fig. 1 Fluorescence observations of cargo transport by motor proteins in living worms. a** Schematics of anterograde and retrograde synaptic cargo transport by kinesin and dynein, respectively, in the DA9 motor neurons of *C. elegans*. **b** Kymograph analysis. Velocity ($v$) was measured as the slope of the trajectory of a fluorescently labeled cargo. The right and left panels, the scale bar is common. **c** Number of synaptic cargos moving anterogradely (A), retrogradely (R), and exhibiting direction change (A→R and R→A). **d** Histogram of the velocity $\{v^i\}$ of synaptic cargos for anterograde (red) and retrograde (blue) transport. **e** Fluorescence micrographs of synaptic cargos (inset). Fluorescence intensity (FI) of synaptic cargos ($n = 133$) (left panel). The distribution of $1/\sqrt{\mathrm{FI}}$ was fitted using a Gamma distribution $b^a x^{a-1} e^{-bx}/\Gamma(a)$ with $a = 6.5$, $b = 0.0050$ (right panel).

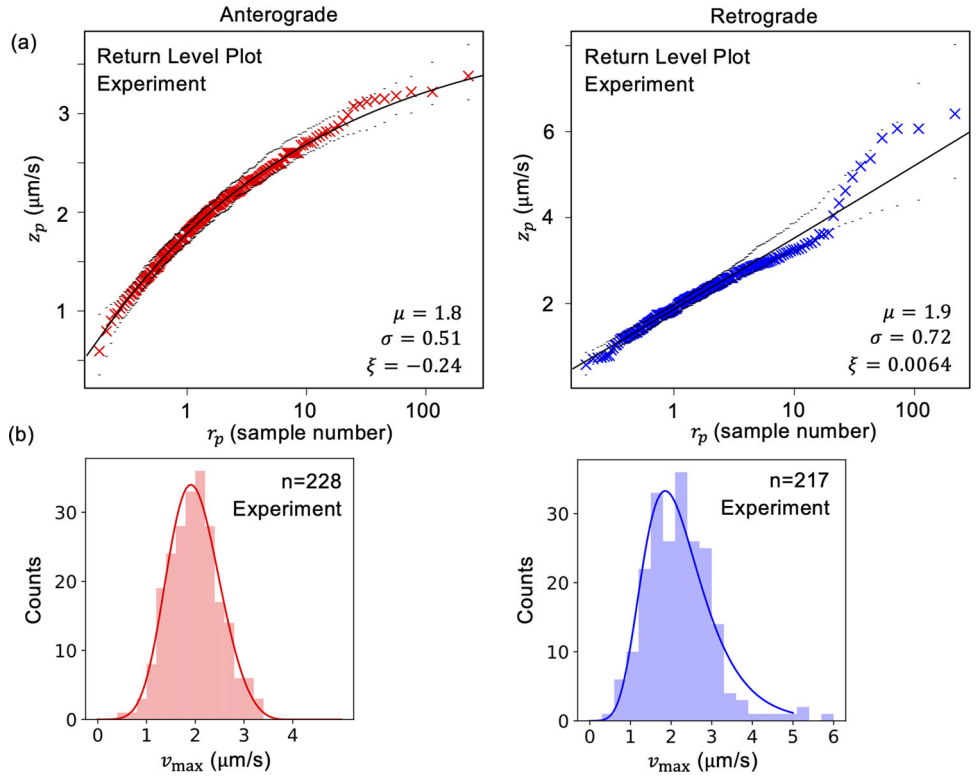


**Fig. 2 Extreme value analysis applied to transport velocity data. a** Return-level plots experimentally measured for anterograde and retrograde transport in the neurons of *C. elegans* worms. The black dotted lines represent the reliable section. **b** Distributions of $v_{max}$ for anterograde and retrograde transport.

distribution ($\xi < 0$), and the extreme value $V_{ex}$ was proved to exist in this case and was estimated to be 4.0±0.4 μm/s using the following equation:

$$V_{ex} = \mu - \sigma/\xi. \quad (2)$$

$V_{ex}$ could be considered as the maximum velocity $V_{max}$ of anterograde transport, a quantity frequently measured in motor protein studies. However, the return-level plot of the retrograde transport (Fig. 2a) shows $\xi \sim 0$, and $V_{ex}$ cannot be estimated using Eq. (2). Figure 2b shows the distributions of $\{v^i_{max}\}(\propto dW(v_{max})/dv_{max})$ for anterograde and retrograde transport.

We checked that the results $\xi < 0$ for anterograde transport and $\xi \sim 0$ for retrograde transport did not depend on the selection of samples from the bootstrapping analysis of the data $\{v^i_{max}\}$ (Fig. S2). We also investigated the block sizes (the number of worms) from which $v^i_{max}$ was selected, which did not affect the result, neither (Fig. S3).

**Construction of a simulation model using the force-velocity relationship**. We considered the behaviors of the return-level plots for anterograde and retrograde transport from the viewpoint of the force-velocity relationship of motor proteins. According to the results of previous studies using single-molecule experiments, two regimes exist in the force-velocity curves of motor proteins: the load-sensitive and load-insensitive regimes[44] (Fig. 3a). In the load-sensitive regime, the velocity changes rapidly with an increase in load ($F$), whereas in the other regime, the velocity changes only slightly with an increase in load ($F$). In vitro single-molecule experiments revealed that the force-velocity curve of kinesin was concave-down[6], whereas some dynein data showed concave-up[9,10,12]. This mechanical difference in the force-velocity relationship can be explained as follows: kinesin keeps moving at a distance of approximately 8 nm along a microtubule (the interval of the microtubule structural unit) per hydrolysis of a single ATP molecule even when a low load is applied, which makes its force-velocity relationship load-insensitive, resulting in a concave-down force-velocity curve. However, some dyneins, whose force-velocity relation shows a concave-up relation and variable step sizes of 8–40 nm under no-load conditions[7,9,11,17], slow down rapidly by decreasing the step size even when a low load is applied, resulting in a rapid velocity decrease and a concave-up force-velocity curve. On the other hand, because several study results show that dynein takes an 8-nm step like kinesin[8,18], in this case, the larger load dependence of the velocity of dynein is explained by the load-dependent kinetic rates. The velocity in the low load condition is written as $v(F)(\mu m/s) \sim v(0) - 0.04F\,(pN)$ for kinesin and $v(F)(\mu m/s) \sim v(0) - 0.2F(pN)$ for dynein from the kinetic rates of the three-state model[45].

The simplest model of the force-velocity curve can be characterized by the changing point $(F_c, v_c)$ between the load-sensitive (thick line in Fig. 3a) and load-insensitive (thin line in Fig. 3a) regimes. Figure 3b describes the multiple motor case. In the following sections, we aim to find the region $(F_c, v_c)$ that reproduce the return-level plots shown in Fig. 2a by performing numerical simulations. Note that the axes of the force-velocity relationship are normalized as $(F/F_s, v/V_{max})$, where $F_s$ is the stall force of a motor protein[6–12], which is the maximum force generated by the motor against an opposing load. We used $(F_s, V_{max}) = (8pN, 4\mu m/s)$ for anterograde transport and $(F_s, V_{max}) = (7pN, 6.5\mu m/s)$ for retrograde transport. The $F_s$ values were obtained from the Ref. [45]. $V_{max}$ for anterograde transport was determined as the extreme value $V_{ex}$ using Eq. (2), and that for retrograde transport was the maximum of the observed experimental velocities as an approximate value of $V_{max}$ because $V_{ex}$ could not be estimated using Eq. (2) in the case of retrograde transport.

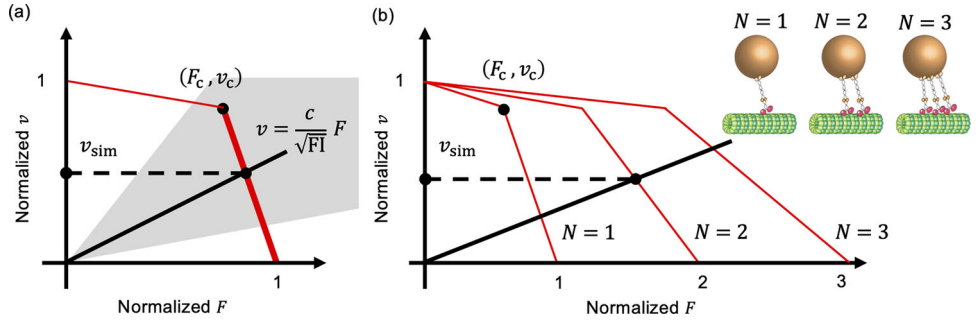


**Fig. 3 Force-velocity relationship for motor proteins. a** Schematics of a concave-down force-velocity relationship of one motor protein. Two regimes, load-insensitive (thin colored line) and load-sensitive (thick colored line) regimes, are represented. The thick black line represents the Stokes' law $v = (c/\sqrt{\mathrm{FI}})F$, where the cargo size $r \propto \sqrt{\mathrm{FI}}$ and $c$ is a constant. The grey area represents the possible values of $c/\sqrt{\mathrm{FI}}$, decided from the experimental velocity values. Normalized *F*: $F/F_s$ and *v*: $v/V_{max}$, where $F_s$ is the stall force of a motor protein. **b** The case of the force-velocity relationship of multiple motors ($N = 3$, where $N$ is the number of motors (Fig. 3b)).

From a given $(F_c, v_c)$, the simulated velocity value $v_{sim}$ is obtained as the intersection between the black line $v = \alpha F$ ($\alpha(= c/\sqrt{\mathrm{FI}})$ representing the Stokes' law and the force-velocity curve $v = f(F)$ ($F = f^{-1}(v)$) of a motor protein (Fig. 3a). The value of $1/\sqrt{\mathrm{FI}}$ is stochastically generated from the Gamma distribution $f_\Gamma(1/\sqrt{\mathrm{FI}})$ (Fig. 1e, right), noting that $\sqrt{\mathrm{FI}} \propto r$ where FI and $r$ are the fluorescence intensity and radius of a cargo, respectively. The constant $c$ is chosen so that the range (=50% interval) of the Gamma distribution multiplied by $c$ corresponds to the range of the measured velocity distribution: $c(F_\Gamma^{-1}(0.5) - F_\Gamma^{-1}(0.05)) = c'(\alpha_{av} - \alpha_{min})$. $F_\Gamma$ is the cumulative distribution of $f_\Gamma(1/\sqrt{\mathrm{FI}})$, $\alpha_{av} = f^{-1}(v_{av})/v_{av}$ and $\alpha_{min} = f^{-1}(v_{min})/v_{min}$ where $v_{av}$ and $v_{min}$ correspond to the mean value and minimum of the measured velocities. $c'$ is a tuning parameter so that the variance of the experimentally measured velocity distribution is similar to the variance of $v_{sim}$. To summarize, we decided $\alpha$ in $v = \alpha F$ so that the distribution of $1/\sqrt{\mathrm{FI}}$ in Fig. 1e represented the variations of the measured velocities (Fig. 1d) approximately. This procedure was repeated 2000 times (*i.e.*, $I = 1,\cdots,n$ where $n = 2000$) (Fig. 4a). Subsequently, $v^i_{sim,max}$ was chosen from among the 10 ($= M$) values of $v_{sim}$.

**Cooperative transport by multiple motors**. It has been suggested that a single cargo can be transported using multiple motors (Fig. 3b). Previously, we used a non-invasive force measurement technique[42,46,47] developed by our research group to examine cargo transport in the neurons of *C. elegans*, and estimated that the number of motors carrying synaptic cargo was 1–3[34]. The frequency $P(N)$ of the number of motors ($N = 1,2,3$) carrying the cargo was approximately $P(1) : P(2) : P(3) = 1 : 2 : 1$, based on the previous observation[34]. After selecting $N$ according to $P(N)$, $v(F/N)$ was used instead of $v(F)$ to determine $v_{sim}$ from the intersection between $v(F/N)$ and the line $v = \alpha F$ (Fig. 3b). The variance in velocity distribution increases in cases of multiple motor transport, as shown in Fig. 4a. This is more representative of experimental conditions than the single motor case shown in Fig. S4.

**Convexity of force-velocity relationships decided by the comparison between the results obtained from the experiment and simulation**. The Kolmogorov-Smirnov statistic $D_{KS}$ is measured for the dataset $\{\hat{v}^i_{sim,max}\}$

$$D_{KS} = \sup_{\hat{v}_{sim,max}} \left| G\left(\hat{v}_{sim,max}\right) - G_n(\hat{v}_{sim,max}) \right| \quad (3)$$

Here, the extreme-value dataset $\{\hat{v}^i_{sim,max}\}$ is the rearranged data of $\{v^i_{sim,max}\}$, such that $\hat{v}^1_{sim,max} \le \hat{v}^2_{sim,max} \le \cdots \le \hat{v}^n_{sim,max}$, and $G_n(\hat{v}_{sim,max})$ is defined as (the number of elements in the sample $\le \hat{v}_{sim,max})/n$. The set of the parameters ($\xi$, $\mu$, $\sigma$) for measured values (Fig. 2 and Table S1) are used to construct $G$ (Eq. (1)). $D_{KS}$ was calculated as the mean value of five trials for each $(F_c, v_c)$.

In the case of anterograde transport, Fig. 4b represents the contour of $D_{KS}$. $D_{KS}$ was smaller when $(F_c, v_c)$ is in the region above the diagonal line (white) of the graph. For the typical case of the region $(F_c, v_c) = (0.8, 0.6)$, Fig. 4c, 4d show the force-velocity relationship $(v^i_{sim}, f^{-1}(v^i_{sim}))$ and the return level plot, respectively (for $v^i_{sim} \ge v_c$, the symbols are marked in pink). Because $\hat{v}^i_{sim,max}$ for a large $r_p$ (pink symbols) was chosen from the load-insensitive regime of the force velocity relationship, it showed convergent behavior, and the graph shows a Weibull-type behavior similar to the experimental one (Fig. 2a). The contour for the shape parameter, $\xi$, of the generalized extreme value distribution for each $(F_c, v_c)$ is plotted in Fig. 4e. The condition $\xi < 0$ is valid for the region above the diagonal line (white) in Fig. 4e. It implied that $\xi$ tends to be negative for the concave-down force-velocity relationship.

Figure 5a–e are the results of the retrograde transport case ($v_{av}$ *and* $v_{min}$, $\xi, \mu, \sigma$ are the measured retrograde ones). Figure 5b represents the contour of $D_{KS}$ (Eq. (3)). In the case of retrograde transport, $D_{KS}$ decreases when $(F_c, v_c)$ is chosen from the region below the diagonal line (white) of the graph. For the typical case of the region $(F_c, v_c) = (0.3, 0.4)$, the force-velocity relationship $(v^i_{sim}, f^{-1}(v^i_{sim}))$ and the return level plots are shown in Figs. 5c and 5d, respectively (for $v^i_{sim} \ge v_c$, the symbols are marked in pink). Unlike the anterograde case, $\hat{v}^i_{sim,max}$ for a large $r_p$ (pink symbols), belonging to the load-sensitive regime of the force velocity relationship, created a gap. Because a small cargo size, which generates a large $\hat{v}^i_{sim,max}$, is a rare event based on the FI distribution (Fig. 1e), the gaps between $\hat{v}^i_{sim,max}$ and $\hat{v}^{i+1}_{sim,max}$ for a large $i$ generated and $\{\hat{v}^i_{sim,max}\}$ was hard to converge in the return level plot in the load-sensitive regime. Note that we discussed the effect of cargo size distributions in the Discussion section (see also Fig. S5). The calculated results for the shape parameter, $\xi$, of the generalized extreme value distribution are plotted in Fig. 5e. $\xi \sim 0$ or $\xi > 0$ is typically observed for the blue region of $(F_c, v_c)$. This implies that $\xi$ tends to be positive for the concave-up force-velocity relationship. Finally, the simulation results for $n = 400$ and $n = 1000$ are shown in Fig. S6, to check that the gaps between $\hat{v}^i_{sim,max}$ and $\hat{v}^{i+1}_{sim,max}$ for a large $i$ did not vanish as the number of samples $n$ becomes large.

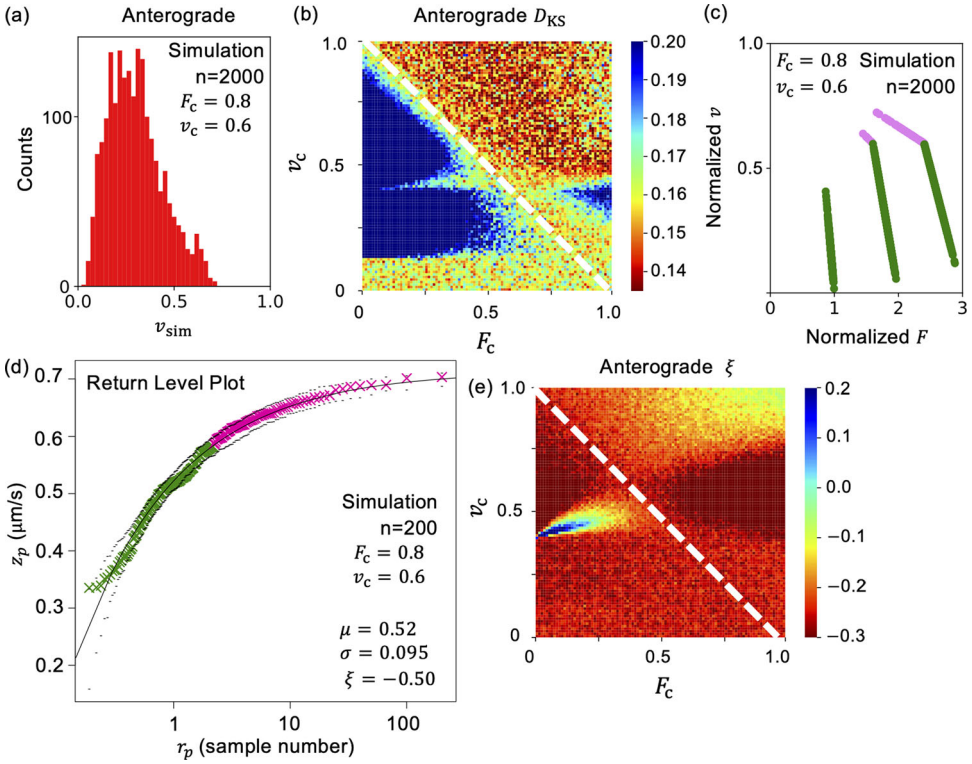


**Fig. 4 Simulation using the force-velocity relationship for anterograde transport. a** Distribution of $v_{sim}$ ($n = 2000$) obtained in the case $(F_c, v_c) = (0.8, 0.6)$, which corresponds to a typical case of a concave-down force-velocity relationship. **b** Contours of $D_{KS}$, defined in Eq. (3). The value of $D_{KS}$ is calculated as the average of five trials. $D_{KS}$ was smaller when $(F_c, v_c)$ is in the region above the diagonal line (white) of the graph. **c** $(v_{sim}, f^{-1}(v_{sim}))$ for $(F_c, v_c) = (0.8, 0.6)$ ($n = 2000$). The symbols are marked in pink (green) for $v^i_{sim} \geq v_c$ ($v^i_{sim} < v_c$). Three lines in the graph represent the multiple motor case depicted in Fig. 3b. **d** Return-level plots of $\{v^i_{sim,max}\}$ ($n = 200$). The symbols are marked in pink (green) for $v^i_{sim} \geq v_c$ ($v^i_{sim} < v_c$). We obtained parameters $\xi$, $\mu$, and $\sigma$ by fitting of Eq. (1) to the graph. **e** Contours of shape parameter $\xi$. The value of $\xi$ is calculated as the average of five trials. $\xi < -0.2$ when $(F_c, v_c)$ is in the region above the diagonal line (white) of the graph.

**Force-velocity relationship of chemo-mechanical coupling models**. We referred to the force-velocity relationship between kinesin and dynein, which is theoretically derived based on the mechanisms underlying ATP hydrolysis by motor proteins. The force-velocity relationships were derived from the three-state model[45]. The force-velocity relationship for the three-state model of ATP hydrolysis is represented as follows:

$$\begin{aligned} v_{three}(F) &= (k_{01} - k_{02})l \\ \frac{1}{k_{01}} &= \frac{1}{\kappa_1} + \frac{1}{\lambda_1} e^{\frac{d_1 F}{k_B T}} \\ \frac{1}{k_{02}} &= \frac{1}{\lambda_2} e^{\frac{-d_2 F}{k_B T}} \end{aligned} \quad (4)$$

See Ref. [45] for the definitions of parameters for both anterograde and retrograde transport. The differences in the model parameters (Eq. (4)) were resulted in the different convexities of the force-velocity relationship (Fig. 6a). Subsequently, the simple force-velocity relationship $v(F)$ depicted in Fig. 3a was replaced with this $v_{three}(F)$. In Fig. 6a, the circles represent the $\{v^i_{sim}\}$ values obtained from the simulations. $\{v^i_{sim,max}\}$ were chosen from $\{v^i_{sim}\}$ ($M = 10$). Using these $\{v^i_{sim,max}\}$, we calculated the return-level plots for the three-state model for $n = 200$,400 and 1000 for anterograde (Fig. 6b) and retrograde (Fig. 6c) transport. We found that the tendency that $z_p$ did not converge for a large $r_p$ in the case of the retrograde transport, *i.e.*, the gaps created between $v^i_{sim,max}$ and $v^{i+1}_{sim,max}$ for a large $i$. This is because a large velocity value is likely to be generated in the case of a concave-up force-velocity relationship, owing to its steep slope in the load-sensitive regime.

## Discussion

We applied EVA to gain insight on the cargo transport by the motor proteins kinesin and dynein in the neurons of living worms, overcoming the limits of in-vivo studies, as observed by high-resolution fluorescence microscopy. We investigated the velocities of the transport and found that the return-level plots of the extreme velocity values revealed differences between the motor protein types. The return level plot of anterograde transport by kinesin shows the typical behavior of a Weibull distribution (the shape parameter $\xi < 0$), where the Weibull type data has a maximum value (Eq. (2)), the counterpart of retrograde transport by dynein does not show a Weibull type behavior (non-negative shape parameter $\xi \sim 0$ or $\xi > 0$). Using the simulation, the abnormality that appeared only for the retrograde velocity data was attributed to the fact that the force-velocity relationship for retrograde transport was concave-up, whereas that for its anterograde counterpart was concave-down. The steep velocity decrease in the low-load condition for the retrograde transport caused a major variation in the larger velocity values, and this behavior tends to generate a major variation in velocity near the maximum velocity and $\xi > 0$ as a result. This abnormal phenomenon occurred because the appearance of large velocity values in the case of small cargo sizes (small values of $\sqrt{\mathrm{FI}}$) was a rare event. When a small cargo size is not a rare event–for example, when the cargo size distribution is uniform unlike the case of the distribution in Fig. 1e–the retrograde velocity data showed a

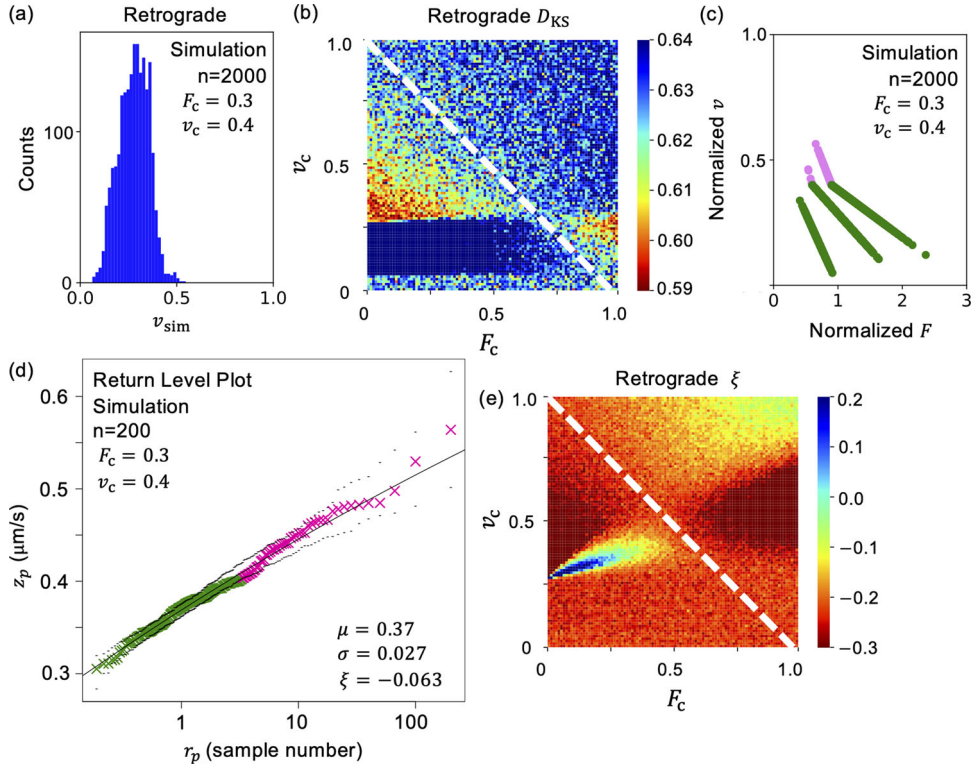


**Fig. 5 Simulation using the force-velocity relationship for retrograde transport. a** Distribution of $v_{sim}$ ($n = 2000$) obtained in the case $(F_c, v_c) = (0.3, 0.4)$, which corresponds to a typical case of a concave-up force-velocity relationship. **b** Contours of $D_{KS}$, defined in Eq. (3). The value of $D_{KS}$ is calculated as the average of five trials. $D_{KS}$ was smaller when $(F_c, v_c)$ is in the region below the diagonal line (white) of the graph. **c** $(v_{sim}, f^{-1}(v_{sim}))$ for $(F_c, v_c) = (0.3, 0.4)$ ($n = 2000$). The symbols are marked in pink (green) for $v^i_{sim} \geq v_c$ ($v^i_{sim} < v_c$). Three lines in the graph represent the multiple motor case depicted in Fig. 3b. **d** Return-level plots of $\{v^i_{sim,max}\}$ ($n = 200$). The symbols are marked in pink (green) for $v^i_{sim} \geq v_c$ ($v^i_{sim} < v_c$). We obtained parameters $\xi$, $\mu$, and $\sigma$ by fitting of Eq. (1) to the graph. **e** Contours of shape parameter $\xi$. The value of $\xi$ is calculated as the average of five trials. $\xi > 0$ when $(F_c, v_c)$ is in the region below the diagonal line (white) of the graph.

Weibull type in the simulation (Fig. S5). No large gaps generated between $v^i_{sim,max}$ and $v^{i+1}_{sim,max}$ even for a large $i$ in this case.

This paper addresses the challenges in applying extreme value statistics to biological systems. Typically, a block size (the number of elements in a block, $M$) of around 1000 is used to obtain a correct extreme value distribution[20]. In comparison, our study uses an extremely small $M$, around 10. This is due to the limited cargo transport observable in a single *C. elegans* worm, resulting in an $M$ value of around 10. The results with a large number ($s$) of worms in order to increase $M$ are presented in Fig S3. We note that in our study we observed variability in vesicle transport velocity obtained from a single worm ($M$ ranges from 5 to 20). Fig. S1 shows the analysis results of experimental data when $M$ was fixed at 5 and 10. In our research, while the parameters $\mu$, $\sigma$, and $\xi$ show dependency on $M$ due to its small size, the qualitative results of $\xi < 0$ for anterograde and $\xi > 0$ for retrograde transport seem to be independent of $M$. The effective use of extreme value statistics in biological experiments, where increasing the sample size represents a challenge, remains an issue for future research.

Recent in vitro single-molecule experiments have suggested a concave-up force-velocity relationship for ciliary[10] and mammalian dynein[9,17], whereas yeast dynein exhibits a concave-down (kinesin-like) force-velocity relationship[7,8]. In the present study, we found a concave-up force-velocity relationship for cytoplasmic dynein in *C. elegans*. To investigate mammalian dynein, EVA was also applied to examine synaptic cargo transport in mouse hippocampal neurons, as originally reported in a previous study[42]. The return-level plot with $\xi > 0$ was also observed for retrograde transport (Figs. S7 and S8), which corresponds to the concave-up force-velocity relationship reported in previous studies[9,17].

Interestingly, several dynein motors exhibit a concave-up force velocity curve. The biological significance of collective cargo transport by multiple motor proteins is explained below and was first introduced in a previous study[17]. When multiple motors work together, the leading dynein decreases its velocity rapidly in the presence of a low load so that the trailing dynein can catch up. This allows the trailing dynein to share the load with the leading dynein, thereby preventing detachment of the leading dynein from the microtubules. In other words, the rapid decrease in velocity in the load-sensitive region results in the self-correction of the position of dynein molecules, allowing them to move as a loosely bunched group[17]. However, the leading kinesin does not slow with regard to the concave-down force-velocity relationship in the presence of a low load. Consequently, the trailing kinesin cannot catch up with the leading kinesin, causing it to easily detach from the microtubules[17]. (Because the load acting on each motor may be different in such multiple-motor cases, there is room to improve the equal load share model between the motors ($F = F_{total}/N$) used in our simulation (Fig. 3b) in reference to previous models[48–51].)

Although the outlines of the in vivo force-velocity relationships could be inferred using the EVA, the stall force values regarding the maximum forces of the motors could not be estimated from this analysis. Many in vitro single-molecule studies have provided the stall force values of kinesin and dynein using optical tweezers[6–12]. Several challenging attempts have made for in-vivo force measurement[52–54].

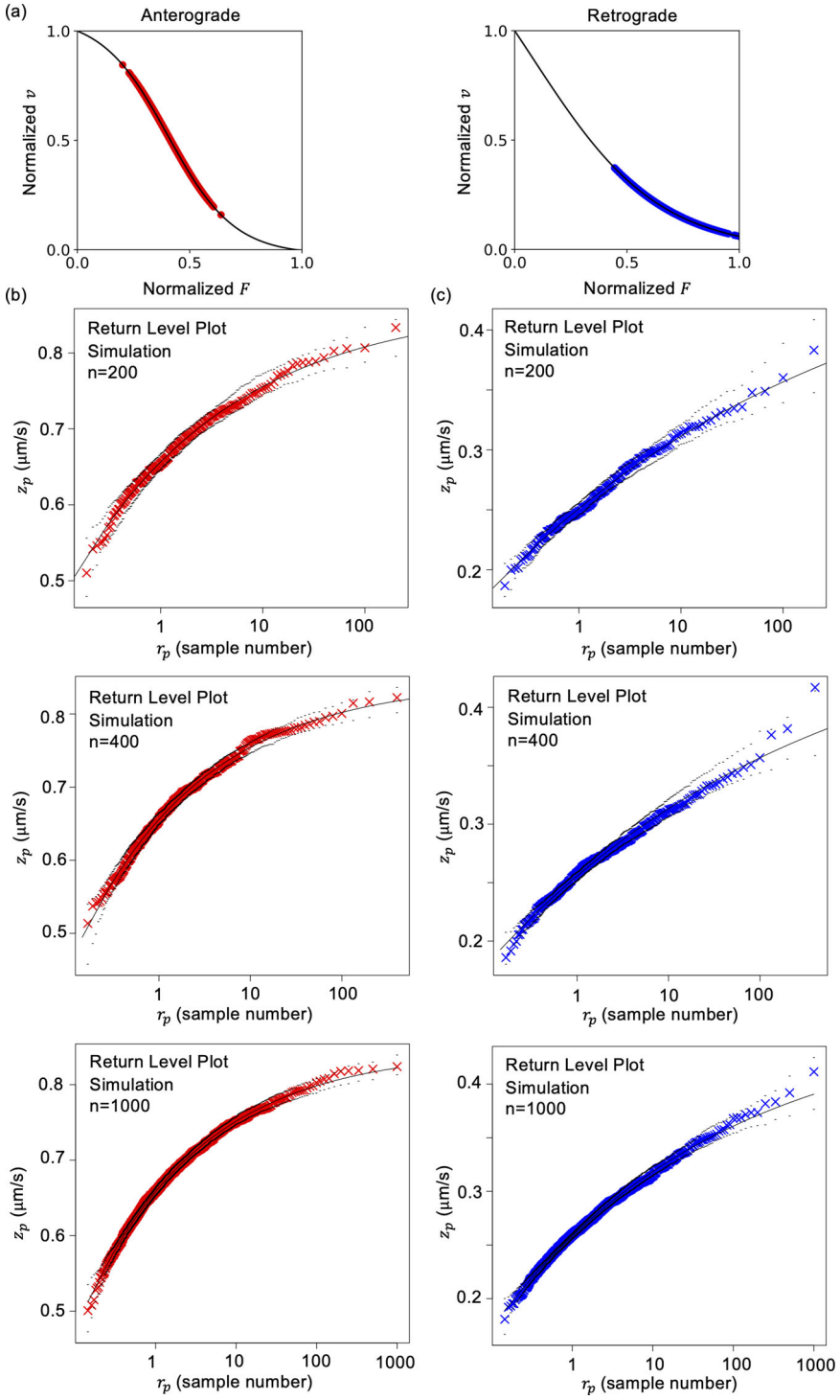


**Fig. 6 Simulation using the force-velocity relationship of the chemo-mechanical coupling model. a** Force-velocity relationship of the three-state chemo-mechanical coupling model (Eq. (4)) (black lines), for anterograde (left panel) and retrograde (right panel) transport. The circles represent $(v_{\mathrm{sim}}, f^{-1}(v_{\mathrm{sim}}))$. Return-level plots of the three-state model (Eq. (4)) for anterograde (**b**) and retrograde (**c**) transport in the cases $n = 200, 400$ and 1000.

In this paper, we attributed the abnormality in the extreme value data for retrograde transport (specifically the rare occurrence of large velocity values and the divergence observed in the return level plot at large $r_p$ values) to a concave-up force-velocity relationship of dynein. However, several mechanisms could lead to the occasional large velocity values in retrograde transport, such as active non-equilibrium fluctuations originating from the cellular cytoskeleton[53,55] and the participation of multiple molecular motors[17]. In the future, we wish to examine not only neurons but also other cell types to further investigate the correlation between the properties of dynein and the behaviour of extreme value data for transport velocity.

Interpretation of return-level plots based on the in vivo force-velocity relationship is a promising tool for future research regarding neuronal diseases, particularly, KIF1A-associated neurological disorders[40,41,56,57]. KIF1A is a type of kinesin

transporting synaptic vesicle precursor cargos, and the force and velocity of the pathogenic mutant KIF1A have been reported to be impaired[56,57]. Since in vivo force measurement is difficult, the estimation of in vivo physical properties using EVA can be helpful for understanding the in vivo behavior of motor proteins. Thus, we believe that the findings of the present study represent a step forward toward broadening the scope of EVA applications.

## Methods

**Sample preparation**. In our study, we used *C. elegans* stains *wyIs251*[Pmig-13::gfp::rab-3; Podr-1::gfp]; *wyIs251* has been previously described[58,59].

*Culture*. *C. elegans* was maintained on OP50 feeder bacteria on nematode agar plates (NGM) agar plates, as per the standard protocol[58,59]. The strains were maintained at 20 °C. All animal experiments complied with the protocols approved by the Institutional Animal Care and Use Committee of Tohoku University (2018EngLMO-008-01, 2018EngLMO-008-02).

**Fluorescence microscopy observations**. A cover glass (32 mm × 24 mm, Matsunami Glass Ind., Ltd., Tokyo, Japan) was coated with 10% agar (Wako, Osaka, Japan). A volume of 20 μL of 25 mM levamisole mixed with 5 μL 200-nm-sized polystyrene beads (Polysciences Inc., Warrington, PA, USA) was dropped onto the cover glass. The polystyrene beads increased the friction and inhibited the movement of worms; levamisole paralyzed the worms. Ten to twenty worms were transferred from the culture dish to the medium on the cover glass. A second cover glass was placed over the first cover glass forming a chamber, thereby confining the worms. The worms in the chamber were observed under a fluorescence microscope (IX83, Olympus, Tokyo, Japan) at room temperature. Images of a GFP (green fluorescence protein)-labelled synaptic cargos in the DA9 motor neuron were obtained using a 150× objective lens (UApoN 150x/1.45, Olympus) and an sCMOS camera (OLCA-Flash4.0 V2, Hamamatsu Photonics, Hamamatsu, Japan) at 10 frames per second.

**Error of $V_{\max}$**. The mean ($\bar{V}_{\max}$) and error ($\delta V_{\max}$) of $V_{\max}$ were estimated from the fitting parameters $\mu(=\bar{\mu}\pm\delta\mu)$, $\sigma(=\bar{\sigma}\pm\delta\sigma)$ and $\xi(=\bar{\xi}\pm\delta\xi)$ of the Weibull distributions defined by Eq. 1 in the main text as follows:

$$V_{\max}=\left(\bar{\mu}-\frac{\bar{\sigma}}{\bar{\xi}}\right)\pm\sqrt{(\delta\mu)^2+\left(\frac{\delta\sigma}{\bar{\xi}}\right)^2+\left(\frac{\bar{\sigma}\delta\xi}{\bar{\xi}^2}\right)^2}.$$

**Bootstrapping method**. A part ($r$: ratio) of the data $\left\{v^i_{\max}\right\}$ $(i=1,\cdots,N)$ was randomly selected, and then the fitting parameters of $\mu$, $\sigma$ and $\xi$ in Eq. (1) were calculated for the partial data. (Here, duplication of the same data was allowed if it was selected.) This procedure was repeated 10 times, and then the errors of $\mu$, $\sigma$ and $\xi$ were calculated. In Fig. S2, each parameter is plotted as a function of $r$ in the cases of anterograde and retrograde transport. The values were stable for a wide range of $r$ $(0.6\le r\le 1)$.

**Block size**. We investigated the dependence of the fitting parameters ($\mu$, $\sigma$ and $\xi$) on the number ($s$) of worms (block size), from which $v^i_{\max}$ was chosen, as shown in Fig. S3. See also Fig. S1 for the return level plots in the case $M$ is fixed ($M=5$ and $M=10$), where $M$ is the number of elements in a block.

**Reporting summary**. Further information on research design is available in the Nature Portfolio Reporting Summary linked to this article.

## Data availability

Data supporting the findings of this study are available within the article and its Supplementary Information files, and also from the corresponding author on reasonable request.

## Code availability

From EVA by using the ismev and evd packages in R[43], we obtained parameters of the generalized extreme value distribution $\xi$, $\mu$, and $\sigma$ in Eq. (1).

Received: 9 May 2022; Accepted: 20 January 2024;
Published online: 13 February 2024

## References

1. Huxley, H. & Hanson, J. Changes in the cross-striations of muscle during contraction and stretch and their structural interpretation. *Nature* **173**, 973–976 (1954).
2. Huxley, A. F. & Niedergerke, R. Structural changes in muscle during contraction; interference microscopy of living muscle fibres. *Nature* **173**, 971–973 (1954).
3. Hirokawa, N., Noda, Y., Tanaka, Y. & Niwa, S. Kinesin superfamily motor proteins and intracellular transport. *Nat. Rev. Mol. Cell Biol.* **10**, 682–696 (2009).
4. Vale, R. D. The molecular motor toolbox for intracellular transport. *Cell* **112**, 467–480 (2003).
5. Okuno, D., Iino, R. & Noji, H. Rotation and structure of FoF1-ATP synthase. *J. Biochem* **149**, 655–664 (2011).
6. Schnitzer, M. J., Visscher, K. & Block, S. M. Force production by single kinesin motors. *Nat. Cell Biol.* **2**, 718–723 (2000).
7. Gennerich, A., Carter, A. P., Reck-Peterson, S. L. & Vale, R. D. Force-induced bidirectional stepping of cytoplasmic dynein. *Cell* **131**, 952–965 (2007).
8. Toba, S., Watanabe, T. M., Yamaguchi-Okimoto, L., Toyoshima, Y. Y. & Higuchi, H. Overlapping hand-over-hand mechanism of single molecular motility of cytoplasmic dynein. *Proc. Natl Acad. Sci. USA* **103**, 5741–5745 (2006).
9. Elshenawy, M. M. et al. Cargo adaptors regulate stepping and force generation of mammalian dynein-dynactin. *Nat. Chem. Biol.* **15**, 1093–1101 (2019).
10. Hirakawa, E., Higuchi, H. & Toyoshima, Y. Y. Processive movement of single 22S dynein molecules occurs only at low ATP concentrations. *Proc. Natl Acad. Sci. USA* **97**, 2533–2537 (2000).
11. Mallik, R., Carter, B. C., Lex, S. A., King, S. J. & Gross, S. P. Cytoplasmic dynein functions as a gear in response to load. *Nature* **427**, 649–652 (2004).
12. Brenner, S., Berger, F., Rao, L., Nicholas, M. P. & Gennerich, A. Force production of human cytoplasmic dynein is limited by its processivity. *Sci. Adv.* **6**, eaaz4295 (2020).
13. Rondelez, Y. et al. Highly coupled ATP synthesis by F1-ATPase single molecules. *Nature* **433**, 773–777 (2005).
14. Watanabe, R., Iino, R. & Noji, H. Phosphate release in F1-ATPase catalytic cycle follows ADP release. *Nat. Chem. Biol.* **6**, 814–820 (2010).
15. Toyabe, S. et al. Nonequilibrium energetics of a single F1-ATPase molecule. *Phys. Rev. Lett.* **104**, 198103 (2010).
16. Toyabe, S., Watanabe-Nakayama, T., Okamoto, T., Kudo, S. & Muneyuki, E. Thermodynamic efficiency and mechanochemical coupling of F1-ATPase. *Proc. Natl Acad. Sci. USA* **108**, 17951–17956 (2011).
17. Rai, A. K., Rai, A., Ramaiya, A. J., Jha, R. & Mallik, R. Molecular adaptations allow dynein to generate large collective forces inside cells. *Cell* **152**, 172–182 (2013).
18. Nicholas, M. P. et al. Control of cytoplasmic dynein force production and processivity by its C-terminal domain. *Nat. Commun.* **6**, 6206 (2015).
19. Gilleland, E. & Katz, R. W. extRemes 2.0: An Extreme Value Analysis Package. *J. Softw.* **72**, 1–39 (2016).
20. Coles S. An Introduction to Statistical Modeling of Extreme Values. *Springer, London* (2001).
21. de Haan L., Ferreira A. Extreme Value Theory. *Springer* (2006).
22. Tippett, M. K., Lepore, C. & Cohen, J. E. More tornadoes in the most extreme U.S. tornado outbreaks. *Science* **354**, 1419–1423 (2016).
23. Kratz M. Introduction to Extreme Value Theory. Applications Risk Analysis & Manegament. *Matrix annals*: pp. 591-636 (2017).

24. Songchitruksa, P. & Tarko, A. P. The extreme value theory approach to safety estimation. *Accid. Anal. Prev.* **38**, 811–822 (2006).
25. Einmahl, J. H. & Magnus, J. R. Records in Athletics Through Extreme-Value Theory. *J. Am. Stat. Assoc.* **103**, 1382–1391 (2008).
26. Gembris, D., Taylor, J. G. & Suter, D. Trends and random fluctuations in athletics. *Nature* **417**, 506 (2002).
27. Rootzen, H. & Zolud, D. Human life is unlimited. but short. *Extremes* **20**, 713–728 (2017).
28. Dong, X., Milholland, B. & Vijg, J. Evidence for a limit to human lifespan. *Nature* **538**, 257–259 (2016).
29. Wong, F. & Collins, J. J. Evidence that coronavirus superspreading is fat-tailed. *Proc. Natl Acad. Sci. USA* **117**, 29416–29418 (2020).
30. Basnayake, K. et al. Fast calcium transients in dendritic spines driven by extreme statistics. *PLoS Biol.* **17**, e2006202 (2019).
31. Hall, D. H. & Hedgecock, E. M. Kinesin-related gene unc-104 is required for axonal transport of synaptic vesicles in C. elegans. *Cell* **65**, 837–847 (1991).
32. Otsuka, A. J. et al. The C. elegans unc-104 gene encodes a putative kinesin heavy chain-like protein. *Neuron* **6**, 113–122 (1991).
33. Chen, C. W. et al. Insights on UNC-104-dynein/dynactin interactions and their implications on axonal transport in Caenorhabditis elegans. *J. Neurosci. Res* **97**, 185–201 (2019).
34. Hayashi, K., Hasegawa, S., Sagawa, T., Tasaki, S. & Niwa, S. Non-invasive force measurement reveals the number of active kinesins on a synaptic vesicle precursor in axonal transport regulated by ARL-8. *Phys. Chem. Chem. Phys.* **20**, 3403–3410 (2018).
35. Rasband W. S. ImageJ. *National Institute of Health, Bethesda, Maryland, USA*, http://imagej.nih.gov/ij/ (1997).
36. D'Souza A. I., Grover R., Monzon G. A., Santen L., Diez S. Vesicles driven by dynein and kinesin exhibit directional reversals without external regulators. *bioRxiv* (2022).
37. Gennerich, A. & Schild, D. Finite-particle tracking reveals submicroscopic-size changes of mitochondria during transport in mitral cell dendrites. *Phys. Biol.* **3**, 45–53 (2006).
38. Gross, S. P. Hither and yon: a review of bi-directional microtubule-based transport. *Phys. Biol.* **1**, R1–R11 (2004).
39. Klassen, M. P. et al. An Arf-like small G protein, ARL-8, promotes the axonal transport of presynaptic cargoes by suppressing vesicle aggregation. *Neuron* **66**, 710–723 (2010).
40. Anazawa, Y., Kita, T., Iguchi, R., Hayashi, K. & Niwa, S. De novo mutations in KIF1A-associated neuronal disorder (KAND) dominant-negatively inhibit motor activity and axonal transport of synaptic vesicle precursors. *Proc. Natl Acad. Sci. USA* **119**, e2113795119 (2022).
41. Chiba, K. et al. Disease-associated mutations hyperactivate KIF1A motility and anterograde axonal transport of synaptic vesicle precursors. *Proc. Natl Acad. Sci. USA* **116**, 18429–18434 (2019).
42. Hayashi, K., Miyamoto, M. G. & Niwa, S. Effects of dynein inhibitor on the number of motor proteins transporting synaptic cargos. *Biophys. J.* **120**, 1605–1614 (2021).
43. R. Core Team. R: Alanguage and environment for statistical computinh. R Foundation for Statistical Computing, Vienna, Austria. URL https://www.R-project.org/. (2018).
44. Longoria, R. A. & Shubeita, G. T. Cargo transport by cytoplasmic Dynein can center embryonic centrosomes. *PLoS One* **8**, e67710 (2013).
45. Sasaki, K., Kaya, M. & Higuchi, H. A Unified Walking Model for Dimeric Motor Proteins. *Biophys. J.* **115**, 1981–1992 (2018).
46. Hayashi, K., Tsuchizawa, Y., Iwaki, M. & Okada, Y. Application of the fluctuation theorem for non-invasive force measurement in living neuronal axons. *Mol. Biol. Cell* **29**, mbcE18010022 (2018).
47. Hasegawa, S., Sagawa, T., Ikeda, K., Okada, Y. & Hayashi, K. Investigation of multiple-dynein transport of melanosomes by non-invasive force measurement using fluctuation unit chi. *Sci. Rep.* **9**, 5099 (2019).
48. Furuta, K. et al. Measuring collective transport by defined numbers of processive and nonprocessive kinesin motors. *Proc. Natl Acad. Sci. USA* **110**, 501–506 (2013).
49. Wang, Q. et al. Molecular origin of the weak susceptibility of kinesin velocity to loads and its relation to the collective behavior of kinesins. *Proc. Natl Acad. Sci. USA* **114**, E8611–E8617 (2017).
50. Driver, J. W. et al. Productive cooperation among processive motors depends inversely on their mechanochemical efficiency. *Biophys. J.* **101**, 386–395 (2011).
51. Klumpp, S. & Lipowsky, R. Cooperative cargo transport by several molecular motors. *Proc. Natl Acad. Sci. USA* **102**, 17284–17289 (2005).
52. Hendricks, A. G., Holzbaur, E. L. & Goldman, Y. E. Force measurements on cargoes in living cells reveal collective dynamics of microtubule motors. *Proc. Natl Acad. Sci. USA* **109**, 18447–18452 (2012).
53. Chaubet, L., Chaudhary, A. R., Heris, H. K., Ehrlicher, A. J. & Hendricks, A. G. Dynamic actin cross-linking governs the cytoplasm's transition to fluid-like behavior. *Mol. Biol. Cell* **31**, 1744–1752 (2020).
54. Blehm, B. H., Schroer, T. A., Trybus, K. M., Chemla, Y. R. & Selvin, P. R. In vivo optical trapping indicates kinesin's stall force is reduced by dynein during intracellular transport. *Proc. Natl Acad. Sci. USA* **110**, 3381–3386 (2013).
55. Mizuno, D., Tardin, C., Schmidt, C. F. & Mackintosh, F. C. Nonequilibrium mechanics of active cytoskeletal networks. *Science* **315**, 370–373 (2007).
56. Budaitis, B. G. et al. Pathogenic mutations in the kinesin-3 motor KIF1A diminish force generation and movement through allosteric mechanisms. *J. Cell Biol.* **220**, e202004227 (2021).
57. Lam, A. J. et al. A highly conserved 310 helix within the kinesin motor domain is critical for kinesin function and human health. *Sci. Adv.* **7**, eabf1002 (2021).
58. Niwa, S. et al. Autoinhibition of a Neuronal Kinesin UNC-104/KIF1A Regulates the Size and Density of Synapses. *Cell Rep.* **16**, 2129–2141 (2016).
59. Wu, Y. E., Huo, L., Maeder, C. I., Feng, W. & Shen, K. The balance between capture and dissociation of presynaptic proteins controls the spatial distribution of synapses. *Neuron* **78**, 994–1011 (2013).


## Acknowledgements

We acknowledge Dr. T. Saigo for facilitating useful discussions regarding EVA and Dr. K. Sasaki for facilitating useful discussions regarding motor proteins. We would like to thank Editage (www.editage.com) for their assistance with English language editing. This work was supported by the JST PRESTO (Grant No. JPMJPR1877), JSPS KAKENHI (grant no. 22K18679), and the FRIS Creative Interdisciplinary Research Program, Tohoku University to K. H., and by JSPS KAKENHI (grant nos. 19H04738, 20H03247, and 20K21378) to S. N.

## Author contributions

K.H. conceived the project with the help of S.N. and wrote the paper. T.N. analyzed the data and performed the simulation. Y.K. and K.N. performed the experiments. S.N. provided the sample.

## Competing interests

The authors declare no competing interests.

## Additional information

**Supplementary information** The online version contains supplementary material available at https://doi.org/10.1038/s42005-024-01538-4.

**Correspondence** and requests for materials should be addressed to Kumiko Hayashi.

**Peer review information** *Communications Physics* thanks the anonymous reviewers for their contribution to the peer review of this work. A peer review file is available.

**Reprints and permission information** is available at http://www.nature.com/reprints

**Publisher's note** Springer Nature remains neutral with regard to jurisdictional claims in published maps and institutional affiliations.